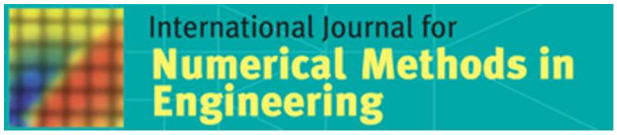

A quasi-static discontinuous Galerkin configurational force crack propagation method for brittle materials

Journal:	*International Journal for Numerical Methods in Engineering*
Manuscript ID	NME-Feb-17-0111.R2
Wiley - Manuscript type:	Research Article
Date Submitted by the Author:	25-Jul-2017
Complete List of Authors:	Bird, Robert; Durham University, School of Engineering and Computing Sciences Coombs, Will; Durham University, School of Engineering and Computing Sciences Giani, Stefano; Durham University, School of Engineering and Computing Sciences
Keywords:	Discontinuous Galerkin, configurational force, rp-adaptivity, crack propagation

INTERNATIONAL JOURNAL FOR NUMERICAL METHODS IN ENGINEERING
Int. J. Numer. Meth. Engng 2016; **00**:1–23
Published online in Wiley Online Library (wileyonlinelibrary.com). DOI: 10.1002/nme

A quasi-static discontinuous Galerkin configurational force crack propagation method for brittle materials

R. E. Bird*, W. M. Coombs & S. Giani

School of Engineering and Computing Sciences, Durham University, Science Site, South Road, Durham, DH1 3LE, UK.

SUMMARY

This paper presents a framework for r-adaptive quasi-static configurational force (CF) brittle crack propagation, cast within a discontinuous Galerkin (DG) symmetric interior penalty (SIPG) finite element scheme. Cracks are propagated in discrete steps, with a staggered algorithm, along element interfaces which align themselves with the predicted crack propagation direction. The key novelty of the work is the exploitation of the DG face stiffness terms existing along element interfaces to propagate a crack in a mesh independent r-adaptive quasi-static fashion, driven by the CF at the crack tip. This adds no new degrees of freedom to the data structure. Additionally as DG methods have element specific degrees of freedom, a geometry driven p-adaptive algorithm is also easily included allowing for more accurate solutions of the CF on a moving crack front. Further, for non-determinant systems, we introduce an average boundary condition that restrains rigid body motion leading to a determinant system. To the authors' knowledge this is first time such a boundary condition has been described. The proposed formulation is validated against, single and multiple crack problems with single-and mixed-mode cracks, demonstrating the predictive capabilities of the method. Copyright © 2016 John Wiley & Sons, Ltd.

Received . . .

KEY WORDS: crack propagation; configurational force; rp-adaptivity; discontinuous Galerkin.

1. INTRODUCTION

Recently, there has been significant interest in the numerical prediction of crack propagation. However, despite numerous frameworks being proposed, accurate and efficient simulation of crack probation is still one of the most challenging problems in solid mechanics. The fracture mechanics community requires algorithms that can predict the evolution of cracks from initiation through to large-scale propagation. In this paper we present an algorithm based on the concept of configurational forces (CF) combined with a discontinuous Galerkin (DG) numerical framework that allows for efficient brittle crack propagation in two dimensions.

The work of Eshelby [15, 16], Rice [60] and Irwin [30, 29], are fundamental to all work in this field. The local variational formulations in [38, 19, 34, 20, 70, 71, 39] use a CF acting at a crack tip to describe the propagation of a crack. CF values have been determined numerically at static fracture fronts by [69, 11, 45, 25]. Using the CF to describe a moving fracture front was initially attempted by Mueller and Maugin [46] within the conventional finite-element context and Larsson and Fagerström [37, 17] in XFEM, with an optimally convergent DG-XFEM achieved by [66]. Later a robust r-adaptive technique was defined by Miehe and co workers [44, 43, 18] for propagating cracks which was also taken to three dimensions by [33]. Futhermore, the framework has recently

*Correspondence to: School of Engineering and Computing Sciences, Durham University, Science Site, South Road, Durham, DH1 3LE, UK. E: robert.e.bird@durham.ac.uk

been applied to materials with non-linear behaviour, see for example the works of Runesson et al. [63] and Tillberg and Larsson [76] on elasto-plasticity and Näser et al. [48, 47] on time-dependent materials and the review by Özenç et al. [51].

An alternative to CF crack propagation is the path independent J-integral [60]. Ishikawa et al. [31] demonstrated the J-integral is the sum of its mode 1 and mode 2 counterparts, from which the respective stress intensity factors (SIF) can be found. The SIF are evaluated seperately by decomposing the stress and displacement field about the crack tip, [78]. The crack direction can then be determined by the maximal principal stress criterion [14]. Mixed mode cracks can also be analysed using the 'Gθ method', see [13], in conjunction with the maximum strain energy release rate criterion (MSERRC) [9]. The Gθ can also be used in conjuction with the maximum circumferential stress criterion (MCSC) [14] or the minimum strain energy density criterion (MSEDC) [67]. Further, the virtual crack extension (VCE) method can be used to model mixed mode problems. The VCE method was introduced independently by deLorenzi, [10] and [54, 53, 55, 26, 27].

Hansbo and Hansbo [21, 22] present a crack propagation method, for linear and non-linear elasticity, using DG methods. However, similar to Heintz [24], the crack propagation techniques proposed in these papers do not exploit the face communication at element interfaces that exist in DG methods. This is similar to several continuous Galerkin (CG) methods where the elements are split internally. Arranz et al. [5] very briefly outlined the advantages of using weak element face terms to propagate a crack however they do not provide any algorithm to do so.

The hybrid DG method exploits element interfaces and element specific degrees of freedom to propagate a crack using a cohesive zone, initial works include [42, 28]. However, this method is strongly mesh dependent as the failure criterion is defined across element interfaces rather than nodes at the crack tip. Cracks can therefore only exist at the initialsed boundaries of elements of the orginial mesh, unlike the r-adaptive method provided by [44] where the element interfaces adapt and align with the predicted crack direction. Accurate solutions for crack propagation paths can only be obtained with very refined meshes [58]. Hybrid DG methods have also been explored by [49, 58, 77, 57], amongst others. Within the context of cohesive law fracture h- and hp-adaptive schemes, respectively [1] and [74], have been produced for space-time DG methods. Additionally a review of the cohesive laws which drive the traction-separation is provided by [52]. In this paper we combine the mesh independent r-adaptive CF crack propagation method provided by [44] with a DG formulation, to take an advantage of the element specific degrees of freedom along element interfaces to propagate a crack in a mesh independent fashion.

DG methods were first introduced by Reed et al. [59] for solving the neutron transport equation. Richter [61] prompted an extension of the original DG method to elliptical problems including linear convective-diffusion terms. However, the discontinuous approximation was only applied for the convective terms, with mixed methods for the second-order elliptic operators. Bassi and Rebay in [7] introduced the complete discontinuous approximations for both the convective and second-order elliptical operators. A review of the use of DG methods for elliptical problems can be found in [3], from here the SIPG method can be found. In this paper the bilinear weak form for linear hyperelastic problems proposed by [23] is used.

After this introduction the paper is split into 5 further sections. In Section 2 the CF method for fracture propagation is outlined, based on the work of [43, 44, 18]. In Section 3 the DG finite element framework, in which the fracture propagation model is cast, is defined. This includes all weakly applied homogeneous and heterogeneous boundary conditions for linear elasticity. In Section 4 the different methods for calculating the CF are described. Section 5 contains the novel numerical implementation of the CF method within the DG framework using an rp-adaptive scheme. Specifically we exploit the element specific degrees of freedom and the weak interaction between elements, existing as stiffness terms in the global stiffness matrix, to propagate a crack. Also included in Section 5 is a description of the average boundary conditions which are used to make a problem determinant when only tractions are applied to the boundaries. Section 6 presents numerical examples which demonstrate the accuracy of calculating the CF, in terms of both magnitude and

DOI: 10.1002/nme

direction for: static, quasi-static, mode 1 and mixed mode problems. Conclusions are drawn in Section 7.

2. CONFIGURATIONAL FORCE FRACTURE

This section provides the key equations for the small strain description of the CF approach to modelling brittle fracture based on the work of Miehe et al. [44]. The continuous formulation is valid for both 2D and 3D however the discrete formulation is different, see [18, 33] for variations of the 3D discrete formulation within a CG framework.

2.1. *Continuous formulation in space and time*

Consider the homogeneous evolving material body in Figure 1, $\mathscr{B} \subset \mathscr{R}^3$, which has an exterior boundary $\partial\mathscr{B}$, crack lips Γ and crack tip $\partial\Gamma$. The subset $\mathscr{B}_\Gamma = \mathscr{B} \setminus \Gamma \cup \partial\Gamma$ is defined with the crack lips Γ^+ and Γ^- and the surface C encircling the crack front. In the limit $\Gamma^+ \to \Gamma$, $\Gamma^- \to \Gamma$ and $C \to \partial\Gamma$. Finally $\partial\mathscr{B}_\Gamma = \partial\mathscr{B} \cup \Gamma^- \cup \Gamma^+ \cup C$ is a set containing all the boundaries of the problem. Here, $\partial\mathscr{B} = \mathscr{B}_D \cup \mathscr{B}_N \cup \mathscr{B}_T$ where $\mathscr{B}_D$, $\mathscr{B}_N$ and $\mathscr{B}_T$ are the Dirichlet, Neumann and roller boundary conditions respectively.

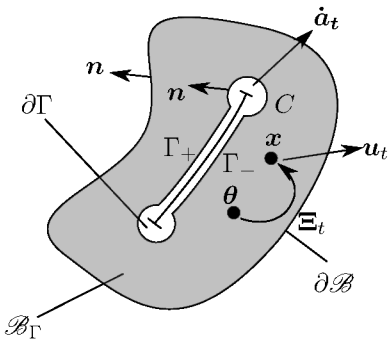

Figure 1. CF quantities defined on the material domain $\mathscr{B}_\Gamma$ (adapted from [44]).

The material points are defined $\boldsymbol{x} \in \mathscr{B}_\Gamma$. They evolve from a set of reference coordinates $\boldsymbol{\theta} \in \Omega$, where $\Omega \subset \mathscr{R}^3$ is the reference domain. This is achieved by using the time dependent mapping $\boldsymbol{\Xi}_t(\boldsymbol{\theta}) = \boldsymbol{x}$ which allows for a change in material structure that reflects the propagation of a crack. The small strain displacement at time $t \in \mathscr{R}^+$ is defined as

$$\boldsymbol{u}_t = \begin{cases} \mathscr{B}_\Gamma \to \mathscr{R}^3 \\ \boldsymbol{x} \to \boldsymbol{u}(\boldsymbol{x})_t. \end{cases} \tag{1}$$

Next we define the global power postulate of the mechanical form of the second law of thermodynamics for power dissipation, $\mathscr{D}$,

$$\mathscr{D} := \mathscr{P} - \frac{\mathrm{d}}{\mathrm{dt}}\Psi \geq 0, \quad \mathscr{P} = \int_{\partial\mathscr{B}} \boldsymbol{t} \cdot \dot{\boldsymbol{u}} \mathrm{d}S \quad \text{and} \quad \Psi = \int_{\mathscr{B}_\Gamma} \hat{\psi}(\boldsymbol{\varepsilon}) \mathrm{d}V. \tag{2}$$

$\mathscr{P}$ is the power applied to the boundary $\partial\mathscr{B}$ by a traction $\boldsymbol{t}$, $\hat{\psi}$ is the free energy function and $\boldsymbol{\varepsilon}$ is the infinitesimal strain

$$\boldsymbol{\varepsilon} = \frac{1}{2}\left[(\partial\boldsymbol{u}_t/\partial\boldsymbol{x})^T + \partial\boldsymbol{u}_t/\partial\boldsymbol{x}\right]. \tag{3}$$

Following the work by Miehe et al. [44], (2_1) becomes

$$\mathscr{D} = \mathscr{P} - \int_{\mathscr{B}_\Gamma} (\boldsymbol{\sigma} : \boldsymbol{\nabla}\boldsymbol{v} + \boldsymbol{\Sigma} : \boldsymbol{\nabla}\boldsymbol{V}) \mathrm{d}V \geq 0, \tag{4}$$

DOI: 10.1002/nme

where $\boldsymbol{\sigma} = \boldsymbol{\nabla}_{\boldsymbol{\varepsilon}}\hat{\psi}(\boldsymbol{\varepsilon})$ is Cauchy stress, $\boldsymbol{\Sigma} = \psi(\boldsymbol{\varepsilon})\boldsymbol{\delta} - (\partial \boldsymbol{u}_t/\partial \boldsymbol{x})^T\boldsymbol{\sigma}$ is the Eshelby stress and $\boldsymbol{\delta}$ is an identity matrix. The boundary conditions for the spacial velocity field $\boldsymbol{v}$ are

$$\boldsymbol{v} \in \{\boldsymbol{v} | \boldsymbol{v} = \bar{\boldsymbol{v}} \text{ on } \partial\mathscr{B}_D\}, \quad \text{where} \quad \boldsymbol{v} = \frac{\partial \boldsymbol{u}_t(\boldsymbol{x})}{\partial t}, \tag{5}$$

which has a prescribed value $\bar{\boldsymbol{v}}$ on a Dirichlet boundary $\partial\mathscr{B}_D$. The boundary conditions for the material velocity field, $\boldsymbol{V}$, are

$$\boldsymbol{V} \in \{\boldsymbol{V} | \boldsymbol{V} \cdot \boldsymbol{n} = 0 \text{ on } \partial\mathscr{B} \cup \Gamma,\ \boldsymbol{V} = \dot{\boldsymbol{o}} \text{ on } \partial\Gamma\}, \quad \text{where} \quad \boldsymbol{V} = \left(\frac{\partial \boldsymbol{\Xi}(\boldsymbol{\theta})}{\partial t}\right) \circ \boldsymbol{\Xi}_t^{-1}(\boldsymbol{x}), \tag{6}$$

with a material velocity $\dot{\boldsymbol{o}}$ at the crack tip. Given that $\boldsymbol{v}$ and $\boldsymbol{V}$ are arbitrary in $\mathscr{B}_\Gamma$ and have boundary conditions (5) and (6) respectively, the following statements of equilibrium can be defined

$$\boldsymbol{\nabla} \cdot \boldsymbol{\sigma} = 0 \text{ in } \mathscr{B}_\Gamma, \quad \boldsymbol{\sigma} \cdot \boldsymbol{n} = \boldsymbol{t} \text{ on } \partial\mathscr{B}, \quad \boldsymbol{\sigma} \cdot \boldsymbol{n} = 0 \text{ on } \Gamma \quad \text{and} \quad \boldsymbol{\nabla} \cdot \boldsymbol{\Sigma} = 0 \text{ in } \mathscr{B}_\Gamma. \tag{7}$$

2.2. *Discrete formulation in space*

A discrete formulation of the power dissipation also exists. This is taken directly from (4) using isoparametric shape functions $\boldsymbol{N_I}$ which act on a node $\boldsymbol{I}$ of element K. $K \in \mathcal{T}$, where $\mathcal{T}$ is a subdivision of the polygonal domain $\mathscr{B}_\Gamma \subset \mathbb{R}^2$ into disjoint triangular elements, with its coordinates mapped into the reference domain using $\boldsymbol{\Xi}_t^{-1}(\boldsymbol{x})$. The nodal material and spacial velocities existing on element K are respectively $\dot{\boldsymbol{D}}_{\boldsymbol{I}}$ and $\dot{\boldsymbol{d}}_{\boldsymbol{I}}$. The derivative of the shape functions in the material domain $\boldsymbol{B_I}(\boldsymbol{x}) = \boldsymbol{\nabla}_{\boldsymbol{x}}\boldsymbol{N_I}$ also exists. Equation (4) can be discretised into the form

$$\mathscr{D} = \sum_{\boldsymbol{I}=1}^{n_{\boldsymbol{I}}} ([\boldsymbol{f_I} + \boldsymbol{p_I}] \cdot \dot{\boldsymbol{d}}_{\boldsymbol{I}} + \boldsymbol{g_I} \cdot \dot{\boldsymbol{D}}_{\boldsymbol{I}}) \geq 0, \tag{8}$$

where $n_{\boldsymbol{I}}$ is the set of all element nodes in the mesh. The conventional force components in (8) are defined as

$$\boldsymbol{f_I} = -\mathbf{A}_{K=1}^{\mathcal{T}} \int_K \boldsymbol{B_I}^{\mathrm{T}} \boldsymbol{\sigma}^h \mathrm{d}V \quad \text{and} \quad \boldsymbol{p_I} = \mathbf{A}_{K=1}^{\mathcal{T}} \int_{\partial K} \boldsymbol{N_I}^{\mathrm{T}} \boldsymbol{t}^h \mathrm{d}V \tag{9}$$

and the CF is

$$\boldsymbol{g_I} = -\mathbf{A}_{K=1}^{\mathcal{T}} \int_K \boldsymbol{B_I}^{\mathrm{T}} \boldsymbol{\Sigma}^h \mathrm{d}V. \tag{10}$$

$\mathbf{A}$, is the usual finite element summation operator. Additionally the material and spacial velocities in element K take the discrete form, denoted by the superscript h,

$$\boldsymbol{V}_t^h = \boldsymbol{N_I}(\boldsymbol{x})\dot{\boldsymbol{D}}_{\boldsymbol{I}} \quad \text{and} \quad \boldsymbol{v}_t^h = \boldsymbol{N_I}(\boldsymbol{x})\dot{\boldsymbol{d}}_{\boldsymbol{I}}, \tag{11}$$

with all interpolation occurring in the material domain, where

$$\dot{\boldsymbol{d}}_{\boldsymbol{I}} \in \{\dot{\boldsymbol{d}}_{\boldsymbol{I}} | \dot{\boldsymbol{d}}_{\boldsymbol{I}} = \bar{\boldsymbol{d}}_{\boldsymbol{I}} \text{ on } \partial\mathscr{B}_D\} \tag{12}$$

is a prescribed displacement on the boundary and,

$$\dot{\boldsymbol{D}}_{\boldsymbol{I}} \in \{\dot{\boldsymbol{D}}_{\boldsymbol{I}} | \dot{\boldsymbol{D}}_{\boldsymbol{I}} \cdot \boldsymbol{n} = 0 \text{ on } \partial\mathscr{B} \cup \Gamma,\ \dot{\boldsymbol{D}}_{\boldsymbol{I}} = \dot{\boldsymbol{o}}_{\boldsymbol{I}} \text{ on } \partial\Gamma\}, \tag{13}$$

where $\dot{\boldsymbol{o}}_{\boldsymbol{I}}$ is the crack tip material velocity. A consequence of (12) is that the following is true

$$\boldsymbol{f_I} = 0 \text{ in } \mathscr{B}_\Gamma, \quad \boldsymbol{f_I} + \boldsymbol{p_I} = \boldsymbol{0} \text{ on } \partial\mathscr{B} \quad \text{and} \quad \boldsymbol{f_I} = \boldsymbol{0} \text{ on } \Gamma. \tag{14}$$

This means that the reduced descritised global power dissipation (8) at the crack tip is

$$\mathscr{D}^h = \sum_{I \in \partial\Gamma} \boldsymbol{g_I} \cdot \dot{\boldsymbol{o}}_{\boldsymbol{I}}. \tag{15}$$

$\boldsymbol{g_I}$ is the CF , it determines crack growth and direction and is calculated in post processing procedure, once the linear elastic system has been solved.

DOI: 10.1002/nme

2.3. Discrete formulation in time

The final step is determining how the crack will propagate. Here we will employ a quasi-static crack propagation framework as presented in [44, 43] to perform a quasi static analysis. First we integrate the discrete dissipation power at the crack, (15), over the time period $[t^n, t^{n+1}]$

$$\Delta\mathscr{D}^h = \int_{t^n}^{t^{n+1}} \mathscr{D}^h \mathrm{d}t \approx \sum_{I\in\partial\Gamma} \boldsymbol{g_I}\cdot\Delta\boldsymbol{o_I}. \tag{16}$$

This gives an incremental constant increase in the crack surface length, $\Delta\boldsymbol{o_I}$, over the time period $[t^n, t^{n+1}]$. It has the form,

$$\Delta\boldsymbol{o_I} = \Delta\gamma_I \frac{\boldsymbol{g_I}}{|\boldsymbol{g_I}|} \quad \text{where} \quad \Delta\gamma_I = \begin{cases} h_o & \text{for } |\boldsymbol{g_I}| \geq g_c \\ 0 & \text{otherwise.} \end{cases} \tag{17}$$

where g_c is a Griffith material failure criteria. h_o is the increase in crack length defined as $h_o = \boldsymbol{g_I}/|\boldsymbol{g_I}|\cdot L_c$, L_c is the original length of the most aligned element face with $\boldsymbol{g_I}/|\boldsymbol{g_I}|$. A crack will propagate the entire reorientated element face associated with L_c. $\Delta\gamma_I$ is subject to the Karush-Kuhn-Tucker conditions

$$\Delta\gamma_I \geqslant 0, \quad (|\boldsymbol{g_I}| - g_c) \leqslant 0 \quad \text{and} \quad \Delta\gamma_I(|\boldsymbol{g_I}| - g_c) = 0. \tag{18}$$

Motion of nodes can be permitted in the material configuration, except motion that would change the shape of the boundary. We recognise that is possible to dissipate power by moving nodes in the material configuration, [75, 64], and thus achieve a minimal energy solution to the problem by increasing the total power dissipated by the term $\sum_{\boldsymbol{I}=1}^{n_{\boldsymbol{I}}} \boldsymbol{g_I}\cdot\dot{\boldsymbol{D}}_{\boldsymbol{I}}$ in (8). However this is a highly non-linear problem and therefore computationally expensive. We therefore do not solve for it here, consistent with the works of [43, 44, 18, 21, 22, 25, 5] and many others, but instead recognise it could potentially improve our solutions. Here, we only consider power dissipation in the form of surface generation, or crack propagation, when the Griffith failure criterion $|\boldsymbol{g_I}| > g_c$, is satisfied at a crack tip.

The key equations for modelling brittle fracture propagation based on CF have now been outlined. Their values are calculated in a post-processing procedure once the linear elastic system for small strain problems has been solved. The linear elastic system is cast within a DG framework presented in the next section. It should also be stated that it is possible to simultaneously solve for the CF and material velocity as in [33], based on the works of [35]. However, there is debate in the literature on the validity of linearising the CF in these approaches [40].

3. DISCONTINUOUS GALERKIN FINITE ELEMENT APPROXIMATION

We consider the following model problem on a bounded Lipschitz polygonal material domain $\mathscr{B}_\Gamma$ in $\mathbb{R}^2$, with $\partial\mathscr{B}_N \cup \partial\mathscr{B}_D \cup \partial\mathscr{B}_T = \partial\mathscr{B}_\Gamma$. In this section three different boundary conditions are described within the DG formulation. On $\partial\mathscr{B}_D$ Dirichlet boundary conditions are applied, the prescribed displacement on this boundary has a value $\boldsymbol{g}_D$. On $\partial\mathscr{B}_N$ Neumann boundary conditions are applied, here the traction has a value $\boldsymbol{g}_N$. Last a roller boundary condition is applied on $\partial\mathscr{B}_T$, here the tangential component to the boundary surface has a value of zero and the displacement normal to the surface has the value $\boldsymbol{g}_T\cdot\boldsymbol{n}$, where $\boldsymbol{n}$ is the unit vector normal to the boundary. The strong form of the problem with the boundary conditions is defined as

$$\begin{aligned} &\boldsymbol{\nabla}\cdot\boldsymbol{\sigma}(\boldsymbol{u}) = 0 \text{ in } \mathscr{B}_\Gamma, \quad \boldsymbol{\sigma}(\boldsymbol{u})\cdot\boldsymbol{n} = \boldsymbol{g}_N \text{ on } \partial\mathscr{B}_N, \\ &\boldsymbol{u} = \boldsymbol{g}_D \text{ on } \partial\mathscr{B}_D, \quad (\boldsymbol{\sigma}(\boldsymbol{u})\boldsymbol{n})\cdot\boldsymbol{n}^{\parallel} = \boldsymbol{0} \text{ on } \partial\mathscr{B}_T \quad \text{and} \quad \boldsymbol{u}\cdot\boldsymbol{n} = \boldsymbol{g}_T\cdot\boldsymbol{n} \text{ on } \partial\mathscr{B}_T \end{aligned} \tag{19}$$

where $\boldsymbol{n}^{\parallel}$ is the tangential unit vector to the boundary. The prescribed values on the respective boundaries, $\boldsymbol{g}_D$, $\boldsymbol{g}_T$ and $\boldsymbol{g}_N$, are the prescribed displacements (fully prescribed $\boldsymbol{g}_D$, and roller $\boldsymbol{g}_T$), and the traction vector $\boldsymbol{g}_N$.

DOI: 10.1002/nme

Each element K of the mesh $\mathcal{T}$, where $\mathcal{T}$ is in general irregular, is the image of the reference triangle under an affine elemental mapping $F_K : \widehat{K} \to K$. We denote by $\mathcal{F}(K)$ the set of the three elemental faces of an element K. If the intersection $F = \partial K \cap \partial K'$ of two elements $K, K' \in \mathcal{T}$ is a segment, we call F an interior face of $\mathcal{T}$. The set of all interior faces is denoted by $\mathcal{F}_I(\mathcal{T})$. Analogously, if the intersection $F = \partial K \cap \partial \mathscr{B}_\Gamma$ of an element $K \in \mathcal{T}$ and $\partial \mathscr{B}_\Gamma$ is a segment, we call F a boundary face of $\mathcal{T}$. The set of all boundary faces of $\mathcal{T}$ is denoted by $\mathcal{F}_B(\mathcal{T})$ and it is the union of the three sets $\mathcal{F}_N(\mathcal{T})$, $\mathcal{F}_D(\mathcal{T})$ and $\mathcal{F}_T(\mathcal{T})$ of faces on the three boundaries $\partial \mathscr{B}_N$, $\partial \mathscr{B}_D$ and $\partial \mathscr{B}_T$ respectively. Additionally the internal crack is represented by tractions on $\partial K \cap \partial \mathscr{B}_N \cap (\Gamma^+ \cup \Gamma^-)$ as zero and the crack tip being represented by an element node existing at $\partial\Gamma$. Moreover, we set $\mathcal{F}(\mathcal{T}) = \mathcal{F}_I(\mathcal{T}) \cup \mathcal{F}_B(\mathcal{T})$. For each element $K \in \mathcal{T}$, we define p_K to be the order of the element. We also define the vector function $\underline{p} = \{ p_K : K \in \mathcal{T} \}$.

For any mesh $\mathcal{T}$ of $\mathscr{B}_\Gamma$ with the degree vector $\underline{p}$, we then define the hp-version discontinuous Galerkin finite element space by

$$W_{\underline{p}}(\mathcal{T}) = \{ \boldsymbol{w} \in [L^2(\mathscr{B}_\Gamma)]^2 : \boldsymbol{w}|_K \in [\mathcal{P}_{p_K}(K)]^2, \ K \in \mathcal{T} \},$$

$[L^2(\mathscr{B}_\Gamma)]^2 = [L^2(\mathscr{B}_\Gamma)] \times [L^2(\mathscr{B}_\Gamma)]$ represents the functional space of the two components of the function $\boldsymbol{w}$ and $\mathcal{P}_{p_K}(K)$ denotes the set of all polynomials on the triangle K of degree no more than p_K. The basis functions chosen are hierarchical, [68], with the test function and displacement described respectively as $\boldsymbol{w} = \boldsymbol{N}_s \boldsymbol{w}_s$ and $\boldsymbol{u}_h = \boldsymbol{N}\boldsymbol{u}_s$. $\boldsymbol{w}_s$ and $\boldsymbol{u}_s$ are the hierarchical basis function coefficients and $\boldsymbol{N}_s$ are the hierarchical functions in the reference element $\hat{K}$.

We now introduce the SIPG method in the bilinear form, for the approximation of the model problem (19): Find $\boldsymbol{u}_h \in W_{\underline{p}}(\mathcal{T})$, such that

$$\boldsymbol{a}(\boldsymbol{u}_h, \boldsymbol{w}) = \boldsymbol{l}(\boldsymbol{w}), \tag{20}$$

for all $\boldsymbol{w} \in W_{\underline{p}}(\mathcal{T})$, where

$$\begin{aligned} \boldsymbol{a}_K(\boldsymbol{u}_h, \boldsymbol{w}) = & \sum_{K \in \mathcal{T}} (\boldsymbol{\sigma}(\boldsymbol{u}_h), \boldsymbol{\epsilon}(\boldsymbol{w}))_K - \sum_{F \in \mathcal{F}_I(\mathcal{T}) \cup \mathcal{F}_D(\mathcal{T})} \langle \{\boldsymbol{\sigma}(\boldsymbol{u}_h)\}, [\![\boldsymbol{w}]\!] \rangle_F \\ & - \sum_{F \in \mathcal{F}_I(\mathcal{T}) \cup \mathcal{F}_D(\mathcal{T})} \langle [\![\boldsymbol{u}_h]\!], \{\boldsymbol{\sigma}(\boldsymbol{w})\} \rangle_F + \sum_{F \in \mathcal{F}_I(\mathcal{T}) \cup \mathcal{F}_D(\mathcal{T})} \beta \langle p_F^2 h_F^{-1} [\![\boldsymbol{u}_h]\!], [\![\boldsymbol{w}]\!] \rangle_F \\ & - \sum_{F \in \mathcal{F}_T(\mathcal{T})} \langle (\boldsymbol{u}_h \cdot \boldsymbol{n})\boldsymbol{n}, \boldsymbol{\sigma}(\boldsymbol{w})\boldsymbol{n} \rangle_F - \sum_{F \in \mathcal{F}_T(\mathcal{T})} \langle \boldsymbol{\sigma}(\boldsymbol{u}_h)\boldsymbol{n}, (\boldsymbol{w} \cdot \boldsymbol{n})\boldsymbol{n} \rangle_F \\ & + \sum_{F \in \mathcal{F}_T(\mathcal{T})} \beta p_F^2 h_F^{-1} \int_F (\boldsymbol{u}_h \cdot \boldsymbol{n})(\boldsymbol{w} \cdot \boldsymbol{n}) \mathrm{d}S, \end{aligned} \tag{21}$$

where β is a penalty term for linear elastic SIPG

$$\beta = \frac{\delta E_Y \nu}{(1+\nu)(1-2\nu)}. \tag{22}$$

In this paper $\delta = 10$, its range is defined by [23], E_Y the material's Young's modulus and ν as Poisson's ratio. Further, h_F is the element face length, and

$$p_F = \begin{cases} \max(p_K^+, p_K^-) & \text{if } F \in \mathcal{F}_I(\mathcal{T}) \\ p_K^+ & \text{if } F \in \mathcal{F}_B(\mathcal{T}) \end{cases} \tag{23}$$

where $\{\cdot\}$, $[\![\cdot]\!]$, $(\cdot,\cdot)$ and $\langle \cdot,\cdot \rangle$ are defined in [4].

The first term on the right hand side of (21) describes the virtual energy in the material bulk. The second is a face stiffness term which averages the jumps in tractions existing between elements. This is followed by its transpose to make the global stiffness matrix symmetric. The fourth term is required to stabilise the method. The last three terms impose the conditions on the boundary $\partial \mathscr{B}_T$

DOI: 10.1002/nme

weakly, the first of the three terms is the weak implementation of the boundary, next is the transpose followed again by a term to stabilise the method.

The right hand side of (20) has the form

$$\begin{aligned} \boldsymbol{l}(\boldsymbol{w}) = &-\sum_{F\in\mathcal{F}_D}\langle \boldsymbol{g}_D, \boldsymbol{n}\cdot\boldsymbol{\sigma}(\boldsymbol{w})\rangle_F + \sum_{F\in\mathcal{F}_D(\mathcal{T})}\beta\langle p_F^2 h_F^{-1}\boldsymbol{g}_D, \boldsymbol{w}\rangle_F + \sum_{F\in\mathcal{F}_N(\mathcal{T})}\langle \boldsymbol{g}_N, \boldsymbol{w}\rangle_F \\ &- \sum_{F\in\mathcal{F}_T(\mathcal{T})}\langle (\boldsymbol{g}_T\cdot\boldsymbol{n})\boldsymbol{n}, \boldsymbol{\sigma}(\boldsymbol{w})\boldsymbol{n}\rangle_F + \sum_{F\in\mathcal{F}_T(\mathcal{T})}\beta p_F^2 h_F^{-1}\int_F (\boldsymbol{g}_T\cdot\boldsymbol{n})(\boldsymbol{w}\cdot\boldsymbol{n})\mathrm{d}S. \end{aligned} \tag{24}$$

The first term is the weak implementation of the Dirichlet boundary condition, followed by its stabilising term. The third term is the implementation of the Neumann boundary condition. The fourth is the boundary condition applied on $\partial\mathscr{B}_T$ followed by its stabilising term. For more information on the implementation of problem (20) we invite the reader to refer to [23].

4. NUMERICAL CALCULATION OF CONFIGURATIONAL FORCE

Here we consider the tip [44, 43] and domain methods [11] for calculating the CF at the crack tip within the SIPG framework. The tip and domain methods are shown in Figures 2a and 2b respectively. The tip method considers only the CF value at the crack tip node, marked as white in Figure 2a. The choice of this node is a result of the power dissipated from crack growth being only associated with CF at this node, as discussed in Section 2.3.

The domain method, shown in Figure 2b, considers the CF on the interior set of nodes, marked as white, of elements within the boundary r_d. The motivation for this choice is that the CF values should be zero on the interior set of nodes, except the crack tip node at $\partial\Gamma$. [11] concluded that spurious CF values exist at interior nodes around the crack tip which should exist at the crack tip. It was found in summing these to the value at the crack tip gave a more accurate solution for the CF. As shown by [29], the stresses close to the crack tip are a function of $r^{-1/2}$, where r is a distance from the crack tip. The finite elements within the discretised space struggle to capture the stress singularity and so the CF, a function of stress, is poorly represented. When using elements which can capture the stress singularities at the tip, [6], the spurious internal material forces become near zero. When singular elements are used in [64], a more accurate CF is obtained compared to using conventional finite elements for their examples.

The equation for calculating the configurational force for the tip and domain method is

$$\boldsymbol{g_I} = -\sum_{n=1}^{n_b}\sum_{K\in A}\int_K \boldsymbol{B_I}^T\boldsymbol{\Sigma}\mathrm{d}V. \tag{25}$$

For the domain method A is the set of elements K which have all their nodes within r_d. For the tip method the set A is the set of all elements K which have a node on $\partial\Gamma$. Finally, n_b is a list of all nodes in A which do not lie on the exterior. The white shaded nodes in Figures 2a and 2b are the interior nodes and crack tip node in the set n_b.

Evaluation of (25) is performed in a post-processing procedure after (21) has been solved.

5. RP-ADAPTIVITY

In this section we describe a method for propagating a crack in quasi-static rp-adaptive procedure using CF fracture mechanics cast within the presented SIPG finite element framework using hierarchical shape functions.

The benefit to using SIPG is the flexibility available to switch off face interactions between elements by removing the DG face stiffness terms from the global stiffness matrix. This creates new surfaces, and is used to propagate a crack. No degrees of freedom (dof) are added to the

DOI: 10.1002/nme

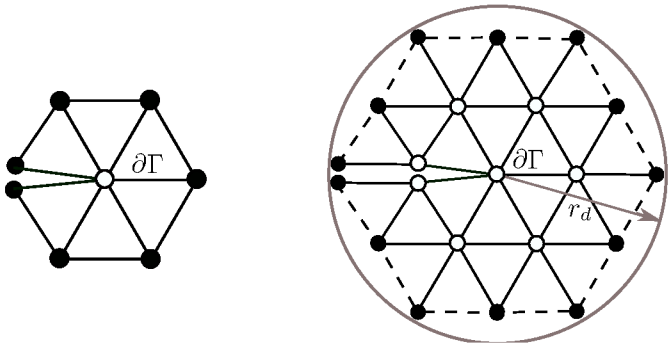

(a) (b)

Figure 2. The mesh around the crack tip $\partial\Gamma$ showing the nodes which are considered in the CF calculation using tip (a) and domain (b) methods.

data structure to propagate a crack whilst only minimal manipulation is required to enable a p-adaptive scheme. The data structure is arranged such that all the dof corresponding to first order components of all elements are numbered first. The labelling of all these dof is unchanged throughout a simulation, as this is the minimum requirement for a finite element discritisation to exist. All subsequent higher order dof are numbered greater than their first order counterparts. An example of the data structure is shown in Figure 3.

5.1. Hierarchical shape functions

In this paper we employ shape functions defined for a reference $\hat{K}$ triangular element in [68] with improved interior bubble functions. An advantage of the adopted shape functions is that values for an arbitrary high order shape function can be created in a hierarchical algorithm. This means it is not necessary to hard code equations for high order shape functions and an element of an arbitrary high order can be generated.

5.2. rp-adaptivity algorithm

In a crack propagation scheme the configurational force, $\boldsymbol{g_I}$, is evaluated at each crack tip using either the tip or domain method. If $|\boldsymbol{g_I}| \geq g_c$, then the crack will propagate in the direction $\boldsymbol{g_I}$ and the rp-adaptivity method will be applied as given in Algorithm 1.

An example of a crack propagating through a mesh, using Algorithm 1, with its corresponding changing global stiffness matrix is shown in Figure 3. The mesh is constructed from 6 elements. For the simplicity of this example only elements sharing a node at the crack tip having a polynomial order, p_K, greater than 1. It is possible to have a group of elements with $p_K > 1$ about the crack tip, these element reside within the radius r_p. An element is considered inside r_p if at least one of its nodes are inside r_p. To propagate a crack, first the linear elastic system is solved producing a stress field. $\boldsymbol{g_I}$ is then calculated from the stress field in the material domain, then following Figure 3:

- Step 1, the element face most aligned with $\boldsymbol{g_I}$ is reorientated about the crack tip to be coincident with $\boldsymbol{g_I}$. The face length has size $h_o = \boldsymbol{g_I}/|\boldsymbol{g_I}|\dot{F}_c$, where F_c is the most aligned element face with $\boldsymbol{g_I}/|\boldsymbol{g_I}|$.
- Step 2, the DG face stiffness terms associated with the reorientated face are removed from the global stiffness matrix. This propagates the crack. Their values reside at the positions highlighted by the black 'X's in the second global stiffness matrix.

This is equivalent to applying homogeneous Neumann boundary conditions on the new crack surfaces. Furthermore the DG face stiffness matrix calculations for this face are also removed

DOI: 10.1002/nme

from any further calculations to prevent any face interaction reappearing. This removes any direct interaction between elements along the face creating a new surface, which extends the boundary of the domain, and propagating the crack.

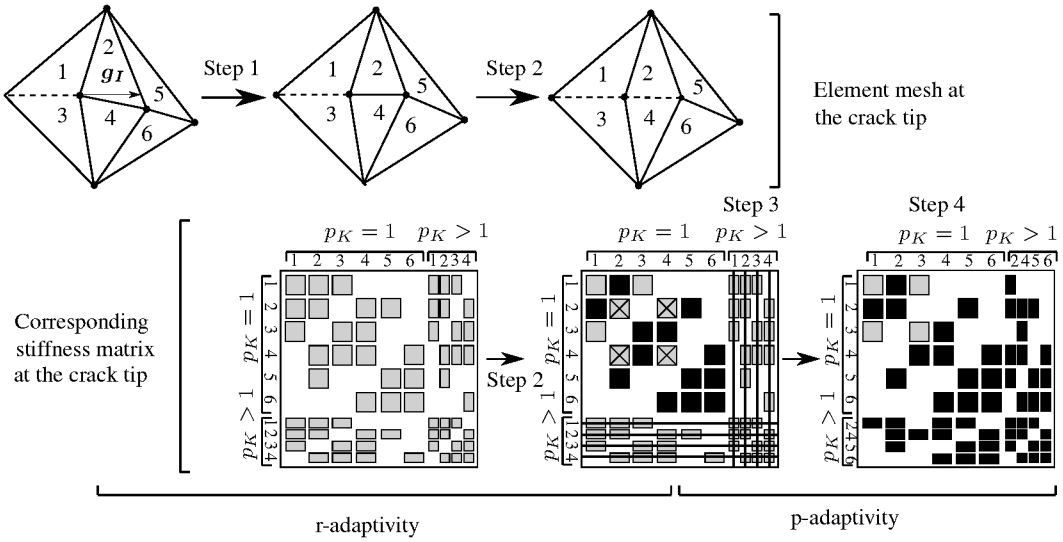

Figure 3. rp-adaptivity for a 6 element mesh at a crack tip, with high order elements at the tip and the corresponding sparsity matrix. The numbers on the rows and columns of the matrices correspond to element numbers in the mesh.

- Step 3, as only elements on the crack tip have a polynomial order greater than 1, and the crack has moved, all rows and columns of the global stiffness matrix associated with the higher order dof of elements no longer at the crack tip are removed.

This is highlighted by the black lines through the final rows and columns of the second stiffness matrix. Additionally, as the geometry of elements which share a node with the new crack tip have also changed, all values associated with these elements' local stiffness are removed. This is represented by the solid black blocks in the second matrix.

- Step 4, the updated local stiffness matrix components of elements are added back into the matrix. This corresponds to element with a changed geometry or increase in polynomial order. All new values are highlighted with black boxes in the third matrix in Figure 3.

The specific detail of the rp-adaptive method which Figure 3 follows is provided in Algorithm 1. The last stage of Algorithm 1 is recalculating the DG area and surface local stiffness matrices for E_r and E_p and adding them back into the global stiffness matrix. When adding new higher order dof, the only constraint is that their numbering is unique to an element, as with all dof in DG.

5.3. Average boundary conditions

This type of boundary condition is used for non-determinant 2D systems. This is the case for linear elastic problems where the displacement is not constrained in both axes. To the author's knowledge this is the first of its kind implemented for a linear elastic problem. These boundary conditions average the displacements in x and y (u and v), and the rotation, to be 0

$$0 = \int_\Omega u \, \mathrm{d}V \approx \sum_{K\in\Omega} \int_K \boldsymbol{N}_u \boldsymbol{u}_K \mathrm{d}V, \quad 0 = \int_\Omega v \, \mathrm{d}V \approx \sum_{K\in\Omega} \int_K \boldsymbol{N}_v \boldsymbol{v}_K \mathrm{d}V \tag{26}$$

and

$$0 = \int_\Omega \left(\frac{\partial v}{\partial x} - \frac{\partial u}{\partial y} \right) \mathrm{d}V \approx \sum_{K\in\Omega} \int_k \boldsymbol{B}_k \boldsymbol{U}_K \mathrm{d}V. \tag{27}$$

DOI: 10.1002/nme

Algorithm 1 rp-adaptivity

Step 1 – r-adaptivity

1: Find nodes within r_d about $\partial\Gamma \rightarrow n_d$.
2: Find interior nodes of the space A, $n_d \rightarrow n_b$.
3: Perform (25) with n_b to obtain $\boldsymbol{g_I}$.
4: Use (17) to get $\boldsymbol{\Delta o_I}$.
5: Create set F, for faces connected to crack node $\partial\Gamma$ with corresponding unit vectors away from crack tip $\boldsymbol{m}$.
6: Identify the most aligned face F_c with $\boldsymbol{\Delta o_I}$ by comparing all $\boldsymbol{m}$ with $\boldsymbol{\Delta o_I}$. Label the most aligned unit vector $\boldsymbol{m}$ as $\boldsymbol{m_c}$, and the corresponding face length L_c:
$F_c = \arg\{\max_{i \in F}(\boldsymbol{\Delta o_I} \cdot \boldsymbol{m}_i)\}$, [43].
7: Reorientate $\boldsymbol{m_c}$ such that $\boldsymbol{m_c} \times \boldsymbol{\Delta o_I} = \boldsymbol{0}$, [43]. Make the reorientated face length $h_o = \boldsymbol{g_I}/|\boldsymbol{g_I}| \cdot L_c$.

Step 2 – Creating a new surface

8: Identify new crack node n_c at the end of face F_c.
9: Remove any further DG face stiffness calculations associated with F_c and delete its values from the global stiffness matrix.
10: Identify all elements with changed vertex coordinates $\rightarrow E_r$.
11: Remove all values in rows and columns, in the global stiffness matrix, for all dof associated with E_r.

Step 3 – p-adaptivity

12: About n_c find nodes within $r_p \rightarrow n_p$.
13: Remove all rows and columns associated with an order $p_K > 1$ for elements not within r_p.
14: Identify elements with $p_k = 1$ which contain nodes n_p and label E_p.

Step 4 – Computation

15: Compute local area and surface stiffness matrices for all dof in set E_r.
16: Compute components of the local area and surface stiffness matrices components associated with a polynomial order > 1 for elements in E_p.
17: Add the newly computed local stiffness matrices components, for $E_r \cup E_p$, to the global stiffness matrix.

Here $\boldsymbol{u}_K$ and $\boldsymbol{v}_K$ are degrees of freedom (dof) corresponding to u and v within element K. $\boldsymbol{u}_K = [u_1, 0, u_2 \ldots u_{ndof}, 0]^{\mathrm{T}}$, $\boldsymbol{v}_K = [0, v_1, 0, v_2 \ldots v_{ndof}]^{\mathrm{T}}$ and $\boldsymbol{U}_K = \boldsymbol{u}_K + \boldsymbol{v}_K$, where $_{ndof}$ is the number of dof of a variable within an element. $\boldsymbol{N}_u$ and $\boldsymbol{N}_v$ are arrays of shape functions, $[N_1, 0, N_2, \ldots N_{ndof}, 0]$ and $[0, N_1, 0, N_2, \ldots N_{ndof}]$ respectively

$$\boldsymbol{B}_K = \left[-\frac{\partial N_1}{\partial y}, \quad \frac{\partial N_1}{\partial x}, \quad \ldots \quad -\frac{\partial N_{ndof}}{\partial y}, \quad \frac{\partial N_{ndof}}{\partial x} \right]. \tag{28}$$

Equations (26) and (27) are incorporated into the global stiffness matrix and thus form part of the solution.

$$\begin{Bmatrix} \boldsymbol{f_n} \\ \boldsymbol{0} \end{Bmatrix} = \begin{bmatrix} \boldsymbol{K} & \boldsymbol{K_{BC}}^{\mathrm{T}} \\ \boldsymbol{K_{BC}} & \boldsymbol{0} \end{bmatrix} \begin{Bmatrix} \boldsymbol{U} \\ \boldsymbol{\alpha_{BC}} \end{Bmatrix}, \quad \boldsymbol{K_{BC}} = \begin{bmatrix} \int_{k_1} \boldsymbol{N}_u \mathrm{d}V & \ldots & \int_{k_{ne}} \boldsymbol{N}_u \mathrm{d}V \\ \int_{k_1} \boldsymbol{N}_v \mathrm{d}V & \ldots & \int_{k_{ne}} \boldsymbol{N}_v \mathrm{d}V \\ \int_{k_1} \boldsymbol{B}_1 \mathrm{d}V & \ldots & \int_{k_{ne}} \boldsymbol{B}_{ne} \mathrm{d}V \end{bmatrix}, \tag{29}$$

where $_{ne}$ is the number of elements, $\boldsymbol{f_n}$ is $\boldsymbol{l}(\boldsymbol{w})$ evaluated at each node, $\boldsymbol{U}$ contains all displacement dof and $\boldsymbol{\alpha_{BC}}$ is a set of arbitrary unknowns that form part of the solution vector.

DOI: 10.1002/nme

6. NUMERICAL EXAMPLES

In this section several crack propagation problems are investigated to demonstrate the accuracy of the SIPG for predicting crack paths against analytical numerical benchmark tests and experimental results. All problems considered in this section assume linear elastic material behaviour. Only small strains in plane strain are present with the free energy function

$$\hat{\psi} = \frac{1}{2}\boldsymbol{\varepsilon}^{\mathrm{T}}(\boldsymbol{C}\boldsymbol{\varepsilon}), \tag{30}$$

where $\boldsymbol{\varepsilon}$ is strain and $\boldsymbol{C}$ is the fourth order stiffness matrix for linear isotropic elasticity. The accuracy of the numerical scheme for predicting a crack propagation path can be evaluated by considering the CF value and direction for mode 1, mode 2 and mixed mode problems.

6.1. Single edge notched static tensile test

This static single edge notched (SEN) test is used to show that SIPG method produces CF values within the range of accuracy obtained in literature, [11, 44]. The value of the CF is dependent on:

- the characteristic mesh size at the crack tip h_{cF};
- the domain around the crack tip where elements have $p_K > 1$ defined by the radius r_p; and
- the radius containing all elements used in the domain evaluation of the CF r_d, (25).

Additionally, r_h is defines the region around the crack tip where elements are of a different length scale to the rest of the mesh. These variables are also shown graphically in Figure 4a.

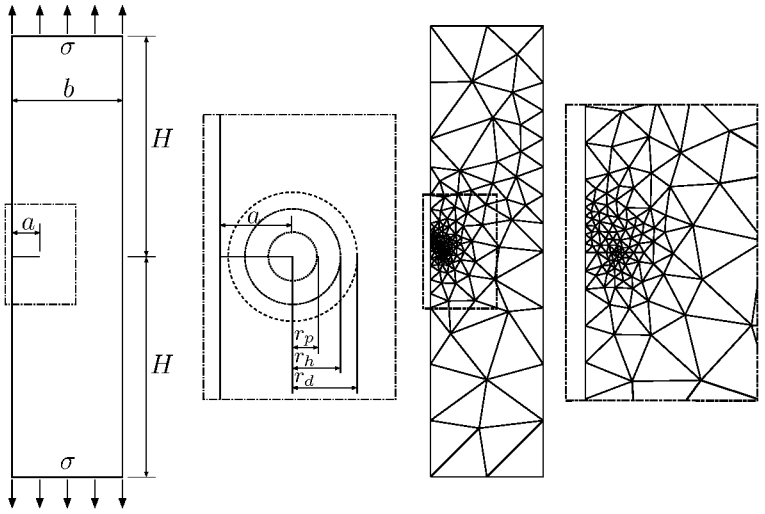

Figure 4. SEN example: (a) geometry and loading conditions of single edge notched specimen. (b) mesh of single edge notched specimen.

The geometry of the test is taken from the benchmark provided by [17] and is shown in Figure 4a. Here the crack length $a = 0.1$ m, the width of the plate $b = 0.5$ m, the half height of the plate $H = 1.0$ m and the uniaxial tensile stress applied is $\sigma = 10$ MPa. The plate has a Poisson's ratio of $\nu = 0.3$ and a shear modulus $\mu = 80$ GPa. Zero average displacement and rotations boundary conditions were applied using (26) and (27). Last, the mesh was generated using the unstructed mesh triangle generator, Triangle [32], and is shown in Figure 4b. All h-refinement occurred in a homogeneous manner uniformly across the entire mesh, as in Figure 5.

DOI: 10.1002/nme

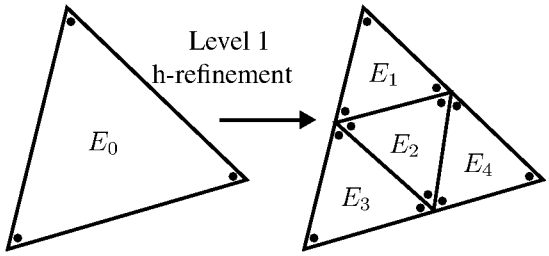

Figure 5. A level 1 homogeneous mesh refinement of triangular element E_0 into 4 new elements. The nodes of the new elements either lie on the middle of the edges, or nodes, of E_0.

An analytical solution of the energy release rate for the plane stress problem, in Figure 4a, for the mode 1 crack path is derived from the J-integral,

$$G = J = \frac{K_I^2(1-\nu)}{2\mu}, \tag{31}$$

where the empirically corrected stress intensity factor, K_I, can be determined from multiple empirical equations provided by [73]. So not to be biased, we choose to define a range in the stress intensity factor, and therefore also the expected energy release rate. The range is provided by the empirical equations which give the smallest and largest K_I values in [73], respectively:

$$\frac{K_I}{K_o} = 0.265\left(1-\frac{a}{b}\right)^4 + \frac{0.857+0.265\frac{a}{b}}{(1-\frac{a}{b})^{\frac{3}{2}}}, \tag{32}$$

and

$$\frac{K_I}{K_o} = \sqrt{\frac{2b}{\pi a}\tan\frac{\pi a}{2b}}\cdot\frac{0.752+0.202\frac{a}{b}+0.37(1-\sin\frac{\pi a}{2b})^3}{\cos\frac{\pi a}{2b}}. \tag{33}$$

Using the stress intensity factor $K_o = \sigma\sqrt{\pi a}$ for an infinite plate with a crack length of $2a$, [29]. The energy release rate for the mode 1 SEN problem is in the range $G \in [256.7, 261.8]$ N/m. As the finite element solutions converge from below for h and p refinements, we will consider $G = 261.8$ N/m as our reference solution and comment all percentage differences from this value, unless stated otherwise. Considering virtual work in the direction of mode crack propagation, the reference mode 1 CF value is $g = 261.8$ N.

6.2. *SEN static tensile test results*

The first investigation was conducted to verify that using SIPG it was possible to obtain accuracies within the range obtained in literature for CF using continuous Galerkin methods, see Table I. Given that the most accurate results obtained in both [44, 11] were obtained using the domain method, this method was used to compute the CF for the problem described in Figure 4a, Section 6.1.

First we investigated how varying r_d around the crack tip affected the accuracy of the CF. For this test $r_h = 0.1$ m and $p_K = 1$ for all elements. The initial element length within r_h was set to 0.04 m and graded to 0.34 m outside r_h. The mesh refinement was uniform, as in Figure 5.

The changes in CF magnitude when considering element rings to compute the domain evaluation of the CF (25), Figure 6, are consistent with the works of [11, 12, 36, 50, 41]. We demonstrate that the CF domain integral, [11], is poorly represented by all refinement levels when only considering elements at the tip (ring 0). This is followed by a large increase in accuracy, $\approx 20\%$ for all refinements. After this initial jump an overall average $\approx 1\%$ increase in accuracy between 1 and 4 rings of elements occurs, however it is noted that increasing the ring size in this region does not guarantee an improvement, and indeed even with refinement an improvement for an element ring size is not guaranteed. For instance [75] exploited the fact that the CF is dependent on the mesh for a mesh improvement strategy. If an increase in the element rings includes a section of poor mesh, the domain evaluated CF could be perturbed leading to a worse result.

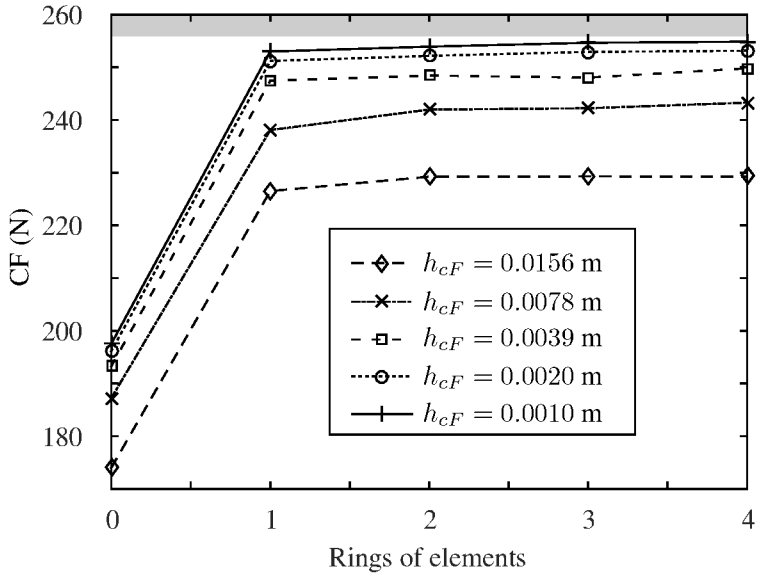

Figure 6. CF magnitude, for different mesh refinements at the crack tip, the range in the empirical solution of g is marked in grey.

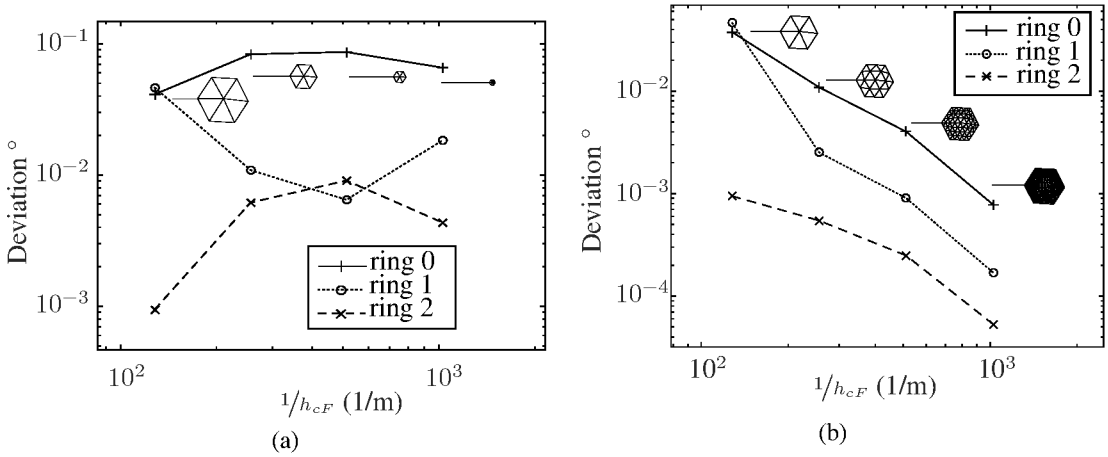

Figure 7. SEN: (a) How the CF derivation angle changes with element size at the crack tip and when considering different rings of elements around the crack tip when computing (25). (b) How CF derivation angle varies when considering the same area of elements, dictated by the element ring area on the coarsest mesh, when computing (25) for different mesh refinements. Example meshes of the elements considered for the computation of the CF are shown for ring 0 in both (a) and (b).

The lack of CF angle convergence, both when increasing element ring size and refining the mesh for a ring size, is demonstrated in Figure 7a. However, when considering a fixed area which is dictated by the element ring size on the most coarse mesh, Figure 7b, monotonic convergence is achieved with uniform homogeneous mesh refinement. The domain integral in its continuous form, [11], is evaluated by considering an area around the crack tip. In the finite element formulation if the area for computing the domain evaluated CF is fixed, and uniform homogeneous refinement occurs, the stress solution will improve in this area. Therefore the domain integral, represented here as the summation of CF nodal values, will improve monotonically.

The next investigation demonstrates how varying element polynomial order around the crack tip affected the accuracy of the CF magnitude with homogeneous mesh refinement. The initial mesh is displayed in Figure 4b. In Figure 8a $r_d = 0.08$ m and $r_p = 0.05$ m, both are kept constant. The

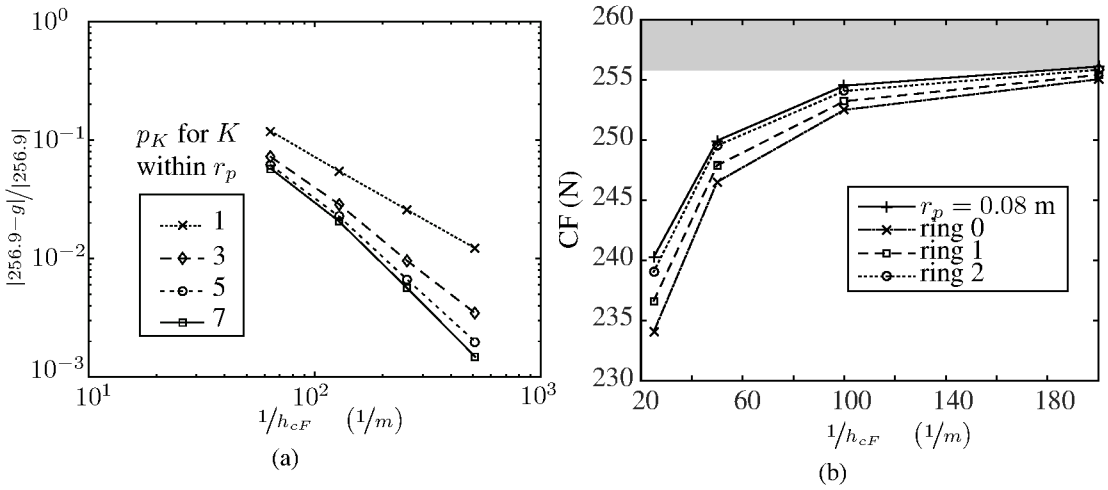

Figure 8. SEN: (a) varying polynomial order, p_K, of elements within $r_p = 0.05$ m, (b) varying the number of $p_K = 5$ elements modelling the stress field around the crack tip for different mesh refinements. The range in the empirical solution of g is marked in grey.

Author	Type of CF evaluation	Element type (order at around tip)	Minimum error (CF magnitude)
Miehe et al. [43, 44]	tip	1^{st}	$2-16\%$
Miehe et al. [43, 44]	domain	1^{st}	$2-8\%$
Bird et al.	tip	1^{st}	2.9%
Bird et al.	domain	1^{st}	2.1%
Bird et al.	domain	3^{rd}	1.6%

Table I. Comparison of error results for calculating the CF at the crack tip for the static SEN problem against methods using a CG framework.

polynomial order p_K of elements within r_p at the crack tip was varied.

In order to demonstrate convergence rates for this problem a value $g = 256.9$ N for the CF was obtained using a structured mesh with greater than 10^6 degrees of freedom with $h_{cF} = 9.8 \times 10^{-5}$ m. This value is within the range presented in Section 6.1 by the empirical equations (32) and (33). Figure 8a demonstrates that refinement in either h or p converges to a CF value of $g = 256.9$ N. For all polynomial orders monotonic convergence was achieved with uniform h-refinement, Figure 5. h-refinement converges more efficiently than p-refinement as the stress is singular at the crack tip [29]. This agrees with the analytical convergence studies obtained in [56, 65] where it was shown for problems with a singularity h-refinement is more efficient than p-refinement. Overall a minimal error of 1.1% for $p_k = 7$ against the upper bound of g.

Last, in Figure 8b, the rings of elements around the crack tip where $p_K = 5$ is varied whilst r_d remains constant at 0.08 m. It demonstrates that the accuracy of the CF solution is more dependent on the rings of elements around the crack which have $p_K = 5$ rather than r_p. By having 2 element rings of high order elements around the tip. The CF error reduces by 7.32% whilst the radius for considering 2 element rings decreases by 8.75 times.

To be consistent the error values in Table I are found using the same empirical solution for this problem found in [43, 44], here $g = 259.1$ N. SIPG obtains results in the range found in literature for CF values.

6.3. Single edge notched quasi-static crack propagation test

The SEN quasi-static crack propagation test, presented here, has the same geometry as the previous section. Here, weakly imposed heterogeneous Dirichlet boundary conditions are applied for a

DOI: 10.1002/nme

displacement of 0.01 m at the top and bottom of the specimen. These act in place of the uniaxial tensile stress shown in Figure 4b. The specimen had a Griffith failure criterion $g_c = 1000$ N/m. The mesh is shown in Figure 9c, with an element length graded from 0.04 m around the expected crack path to 0.35 m. For this test $r_p = 0.08$ m and $r_d = 0.1$ m, the domain of elements with a higher polynomial order moved with the crack tip.

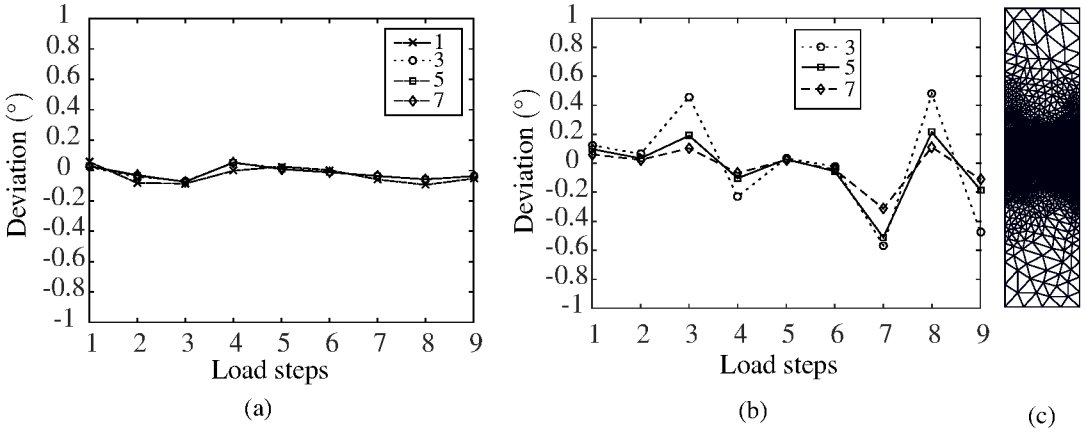

Figure 9. SEN crack propagation direction: (a) using the domain method, [11], to calculate g_I, (b) using the tip method to calculate g_I, [43], and (c) the initial mesh used for both (a) and (b).

The results for the instantaneous CF deviation from the expected crack direction, of $0°$, are shown in Figures 9a and 9b. Each figure shows a total of 8 element face separations. This equates to a total crack path length across the plate of 0.31 m and 0.30 m, for Figures 9a and 9b respectively. The figures demonstrate the improvements gained by using the domain approach. The domain method obtained a maximum difference, from $0°$, of $0.09°$ compared to the tip evaluation which achieved $0.55°$. The figures show how the path direction is governed by integration scheme more than the polynomial order of elements around the tip. The average difference between $p_K = 1$ and $p_K = 7$ for the domain approach was $0.029°$, and for the tip approach was $1.86°$.

6.4. Double notched two holed quasi-static crack propagation test

This benchmark taken from [9], is a tension test of a double edge notched specimen with two holes for mixed mode problems, the geometry and loading conditions are shown in Figure 10a. This

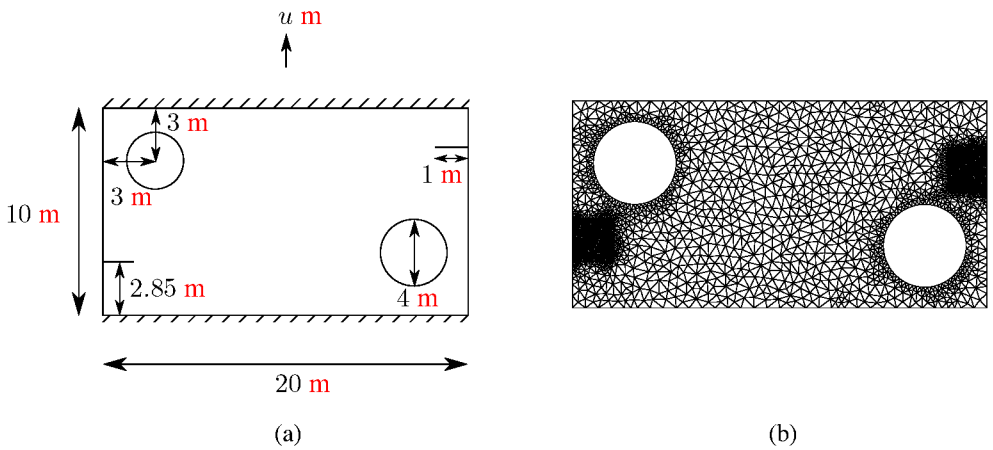

Figure 10. Double crack and hole example: (a) geometry for the two holed quasi-static crack propagation test and (b) starting mesh with element length of 0.3 m refined to 0.015 m at the crack tips.

DOI: 10.1002/nme

test is necessary to show that SIPG can produce accurate results, compared to CG, for the mixed mode crack propagation problems. The plate acts in plane strain and has a shear modulus $\mu = 8$ GPa, Poisson's ratio $\nu = 0.3$ and a Griffith failure criterion of $g_c = 1000$ N/m. In Figure 10b the mesh is refined around the crack tips as in [43], this is to ensure a more valid comparison. Here

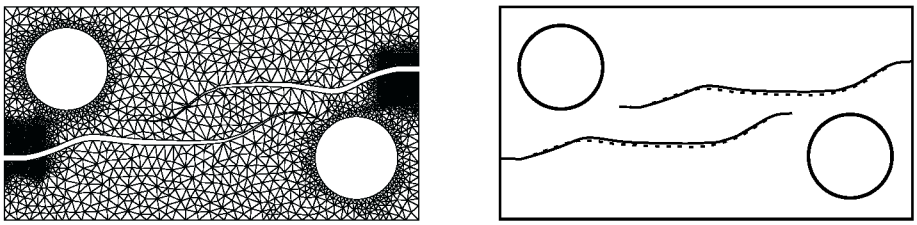

(a) (b)

Figure 11. Double crack and hole example: (a) propagation path and deformed mesh using the domain evaluation method of the CF [64] where the displacements have been magnified by a factor of 10 and (b) a comparison of paths between those obtained in Figure 11a (solid line) and the path obtained by [43] (dashed line).

$r_p = 0.1$ m, with elements of polynomial order of 3 within r_p and 1 elsewhere. The CF domain method [11] with $r_d = 0.2$ m was employed to evaluate this mixed mode problem. The two cracks propagate simultaneously in the same load step. The deformed mesh is shown in Figure 11a. The crack propagation path obtains a good agreement with Miehe et al. [43] as shown in Figure 11b.

A slight variant of the experiment, shown in Figure 11a, was performed with the same material properties, loading conditions, radii r_d and r_p, and polynomial order distribution. The experiment analysed the precision of the crack propagation. As the problem is symmetric the two cracks paths in the problem should have the same normalised position relative to their starting point. The difference in the crack paths is a measure of the precision. The results are displayed in Figure 12a, however it is important to note that the difference in the crack paths is empathise by the x and y axes being different scales. The precision was measured as the maximum percentage difference from the mean

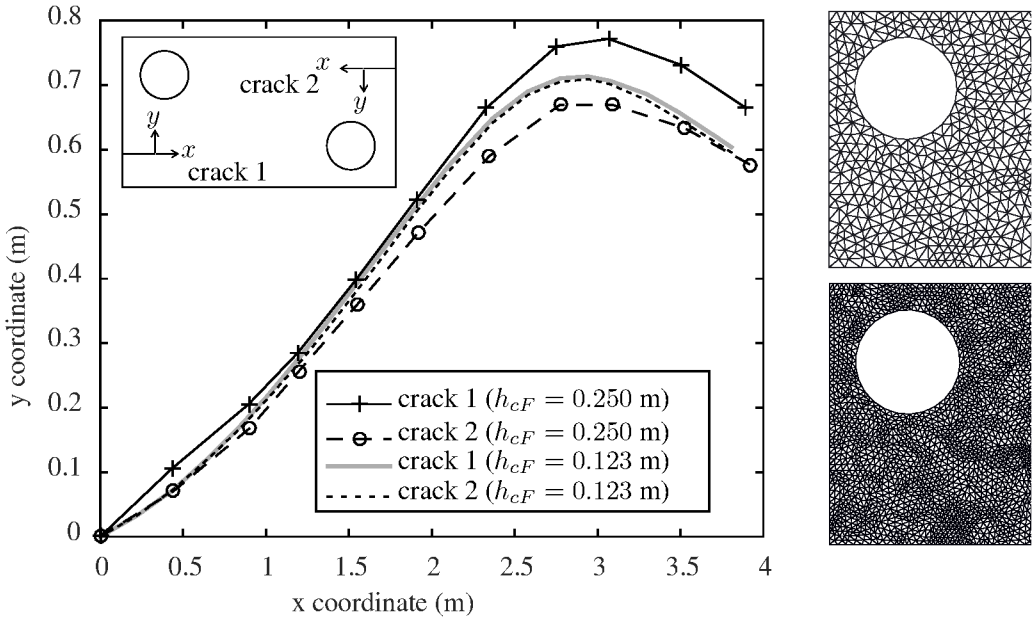

(a) (b)

Figure 12. Double crack and hole example: (a) crack propagation paths for the two different mesh refinements in (b), where $h_{cF} = 0.250$ m (top right), and $h_{cF} = 0.123$ m (bottom right).

of the two crack paths. The coarser mesh, element length of 0.25 m, obtain a precision of 20%. The refined mesh, element length of 0.123 m, achieved a precision of 2%. The lack of precision is caused by two features. First, for a coarse unstructured mesh, the stress field is poorly represented. This means on the first load step the configuration force is unlikely to be the same at both crack tips and so the two cracks will propagate in slightly different directions. Secondly, as the increase in crack length $\Delta \boldsymbol{o}$, is larger for the coarse mesh the error in crack path is magnified. This results in a diverging crack path, Figure 12a, and different stress fields at the tips, Figure 13b. The locations of the new crack tips and the stress fields, Figure 13a, now contrast more than if a finer mesh was used, Figure 12a. Ultimately the difference between the stress fields and the error in crack path compounds the inaccuracy as the crack propagates through the specimen.

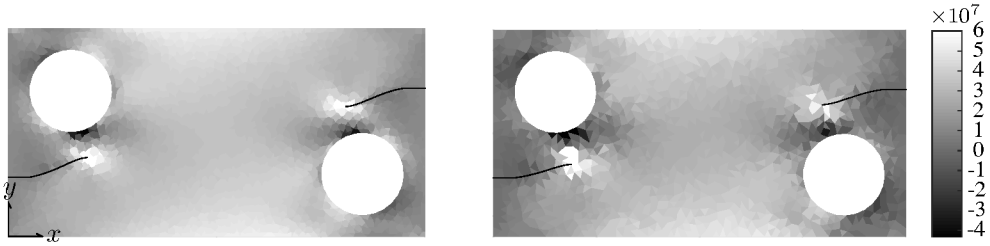

(a) (b)

Figure 13. Double crack and hole example: plot of σ_{xx} (Pa) for (a) $h_F = 0.123$ m and (b) $h_F = 0.250$ m.

6.5. *Mixed mode single crack propagation in a beam*

In this section a mixed mode single crack propagation problem in a double cantilever beam is analysed, the problem was first described by [8]. The problem is described in Figure 14a, it considers a fixed beam with a centre crack where the tip perturbed by a small angle. A traction is applied to the end of beam such that the two halves are pulled apart. The problem acts in plane stress, with $L = 0.3$ m, $h = 0.1$ m, $a = 0.1$ m, $p = 0.175$ N/m, $\Delta x = 7.6$ mm, $g_c = 500$ N/m, $\theta = 5.41°$, $E_Y = 206.8$ GPa, and $\nu = 0.3$. The crack is propagated using (17) with, $r_d = 0.01$ m and $p_K = 2\ \forall K \in \mathcal{T}$. The

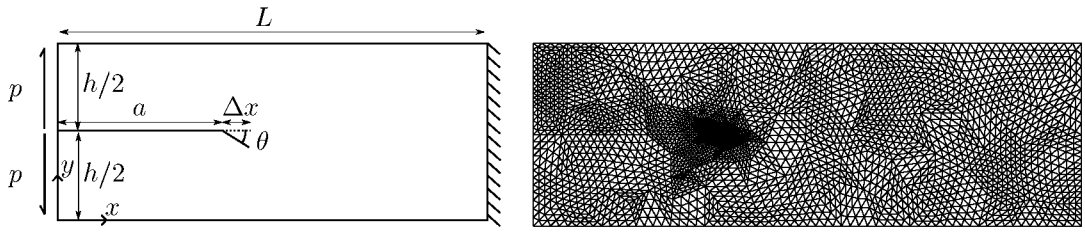

(a) (b)

Figure 14. Crack in a beam problem schematic (a) with the corresponding mesh (b).

crack step is dictated by the side length of elements in the mesh, Figure 14b elements are graded from $1/400$ m at the crack tip to $1/200$ m at the far field. The resultant crack path using (17) with the SIPG face splitting method is compared against the XFEM methods using the maximum circumferential stress criteria (MCSC) [8, 62], and against the cracking particle method which also uses MCSC, [2].

The resultant crack paths are displayed in Figure 14a. It is important to note that the axes are different scales and, the axes are also normalised with respect to the maximum length of the plate in the axes' orientation. Very similar results are obtained between CF SIPG, XFEM MCSC [62], and the cracking particle method MCSC [2]. The only outlier is [8], however the general shape of their crack path is similar. In this paper we choose the CF method, [44], as this method maximises the power dissipation through crack growth, derived from the second law of thermodynamics.

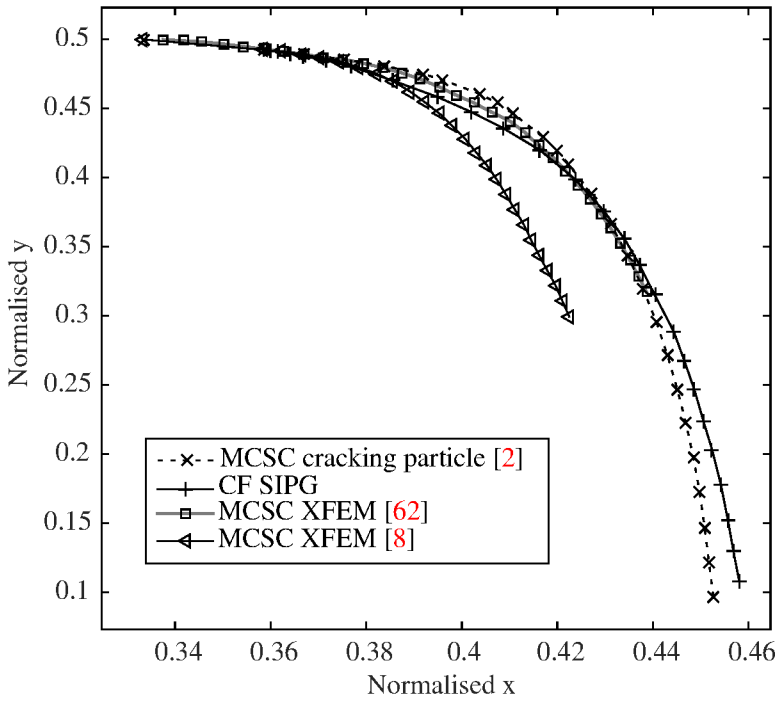

Figure 15. Comparison of crack paths, for the crack in a beam problem 14a, using the SIPG CF crack path criterion (17), XFEM MCSC [8, 62], and the MCSC cracking particle method [2]. The axes x and y correspond to the same orientation as in Figure 14a.

6.6. *Quasi-static cross crack propagation in a finite plate*

The final numerical example is taken from [72], shown in Figure 16a. The example is used here to investigate the consistency in CF values within a numerical experiment for two different boundary conditions, the average boundary conditions presented in Section 5.3 and a fixed bottom left corner node. The plate has a shear modulus $\mu = 8$ GPa, Poisson's ratio $\nu = 0.3$ and a Griffith failure criterion of $g_c = 1000$ N/m. The traction σ acting perpendicular to the plate surface has a value of 10 MPa. The problem is a symmetric plate biaxial loaded, acting in plane strain, with four crack tips orientated in a cross. The cracks are propagated using the r-adaptive method combined with the face splitting algorithm presented in this paper. The increase in crack length for each crack propagation step is the same as the characteristic element size of the mesh, $1/30$ m or $1/50$ m, and corresponds to splitting of one element face. $p_K = 1$ everywhere and the tip method was used to investigate the effect the different boundary conditions had on the CF value at the crack tip node. This ensures that only the boundary conditions can cause any disparity in CF values at the crack tips. It is possible for the domain method to capture a different number of elements around the crack tip depending on the element distribution. Each crack was propagated at the same rate. The mesh generated was structured and symmetric, the mesh before crack propagation is shown in Figure 16b.

Each crack should undergo mode 1 propagation, the CF vector should therefore only have one non-zero component which in this example is parallel with the crack lips. The first investigation is designed to isolate the effect the different boundary conditions have on the CF value at each crack tip. Therefore a symmetric structured mesh is used as in Figure 16b. The magnitude of the deviation of the CF away from its expected direction for each crack tip is represented the by angle between its vector components as shown in Figure 17.

Figure 17 shows that refining from $h_{cF} = 1/30$ m to $h_{cF} = 1/50$ m shows no improvement or even a worse representation of the crack path. The fixed corner makes the problem non-symmetric by introducing a reaction force. Therefore the boundary conditions are not sufficient for pure mode 1 crack propagation hence it is unachievable, even with refinement. However, the boundary condition

DOI: 10.1002/nme

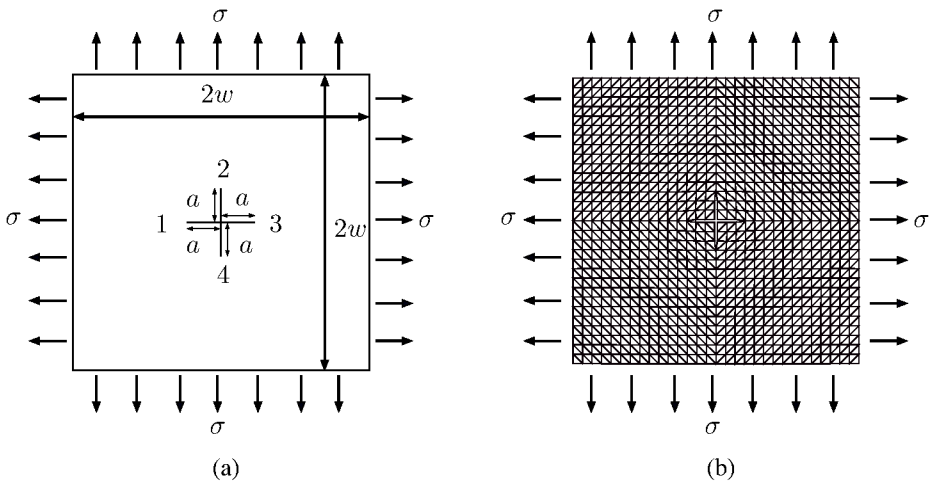

Figure 16. Cross crack: (a) problem geometry where $2w = 1$ m, the cracks at the centre have a length $a = 0.1$ m with the cracks labelled to 1-4. (b) the deformed structured symmetric mesh with element face length $h_{cF} = 1/30$ m before propagation, with the displacement scaled by a factor 10^3.

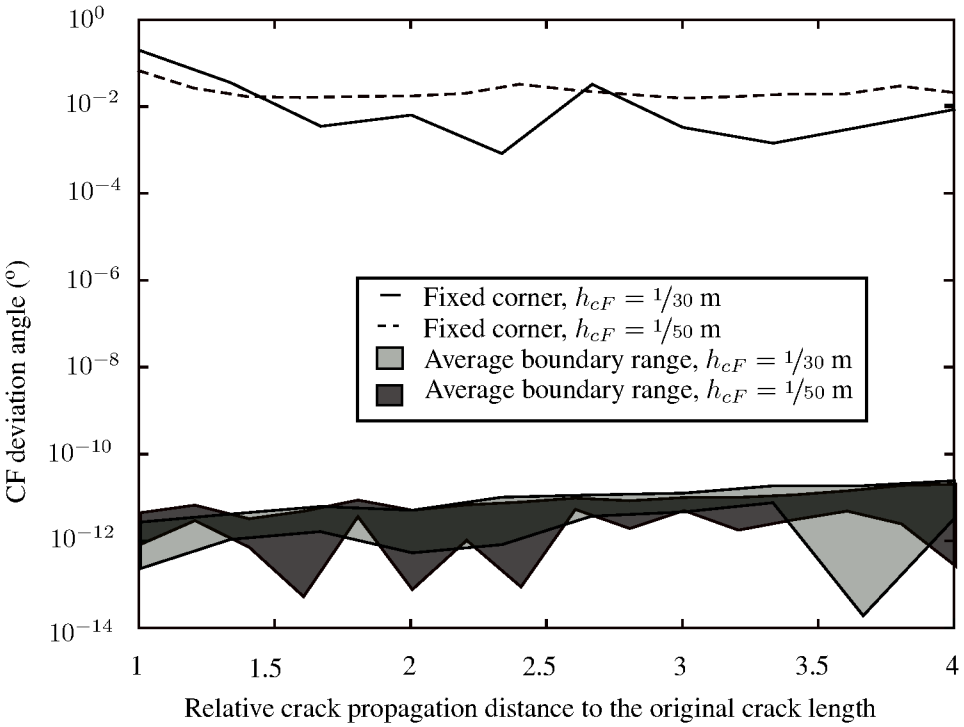

Figure 17. The deviation angle of the CF for a structured homogeneous meshes with the same pattern as in Figure 16b for different element face length $h_{cF} = 1/30$ m and $h_{cF} = 1/50$ m. The results for average and fixed corner boundary condition are displayed.

does conserve symmetry in one respect as the deviation angle is the same for all cracks, within computational accuracy.

The range of the deviation angle for the 4 cracks using the average boundary conditions is shown Figure 17 by the greyed regions in the graph. The crack path deviation is within the order of computational error for both $h_{cF} = 1/30$ m and $h_{cF} = 1/50$ m. The example demonstrates that the

DOI: 10.1002/nme

average boundary conditions are suitable to obtain pure mode 1 fracture. The crack path deviation is at least an order 8 times more accurate than that obtained with the fixed corner boundary condition.

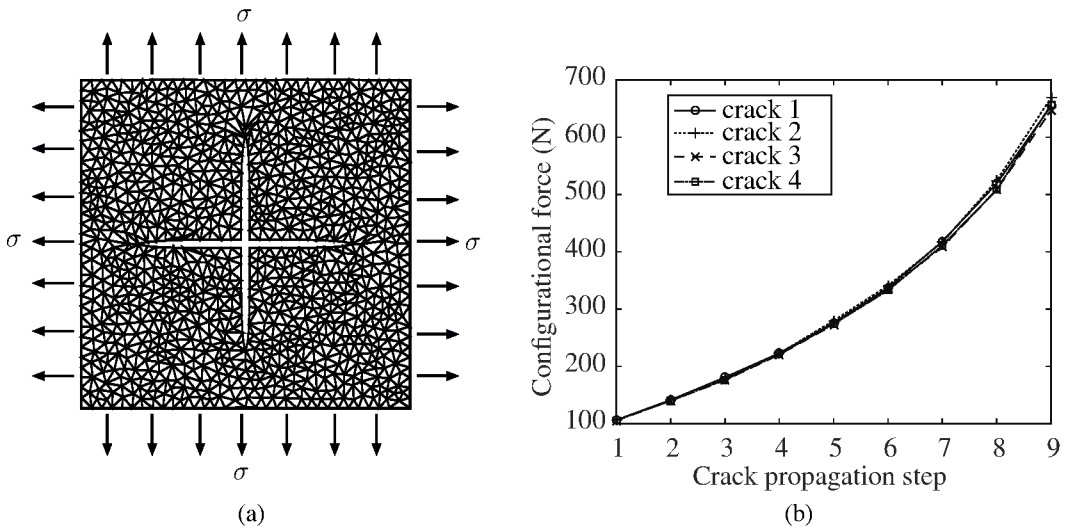

Figure 18. (a): resultant unstructured mesh with element length $1/30$ m after 9 propagation steps with the displacement scaled by a factor of 10^3. (b): mode 1 CF components for each of the 4 cracks.

Finally the norm of the CF values at each of the 4 cracks, see Figure 18b, is compared using an unstructured mesh with average boundary conditions and an average $h_F = 1/30$ m, Figure 18a. The cracks undergo 8 element face splits corresponding to a total crack length increase of ≈ 0.27 m. The percentage difference of the CF, from the average value, for each crack ranges from $\pm 0.39\%$ to $\pm 1.24\%$. For the symmetric mesh in Figure 16b the CF values were found to be the same for each crack. The range here is therefore generated by the non-symmetry of the unstructured mesh. At $a = 0.1$ m the mean CF value is 105.6 N, this is comparable to the XFEM solution calculated in [72] where a value of 102.9 N was obtained, via a J-integral domain evaluation.

7. CONCLUSION

In this paper we have used the thermodynamically consistent framework presented by Miehe and co-workers [43, 44, 18] to model brittle fracture for small strain problems in a SIPG finite element method. The proposed method exploits the element specific degrees of freedom and the weak interaction between elements, and existing as stiffness terms in the global stiffness matrix to propagate a crack in a fashion that is independent of the original element interface orientation. These benefits have not been taken advantage of in the past. In the proposed numerical method a crack is propagated through: (i) moving an element face in line with the CF, (ii) removing the DG face stiffness values, in the global stiffness matrix corresponding to the reorientated face, (iii) recalculating the local stiffness matrices of elements with changed geometry or polynomial order, and, (iv) updating the values global stiffness matrix. This r-adaptive procedure in DG adds no dof to the data structure, only the change of local element stiffness values in the global stiffness matrix is required. Additionally we have presented an algorithm to implement arbitrary high order elements around a moving crack tip and produced an rp-adaptive scheme for SIPG methods. Good agreement for CF values and crack paths was obtained for static and quasi-static, single and mixed mode, problems using the proposed formulation. Mixed mode crack paths using the CF method were also compared against the MCSC method within the numerical framework of XFEM, and the cracking particle method. The comparisons were made from results found in literature using existing finite element methods for the same problems. Finally, for non-determinant systems, we introduce an average boundary condition that restrains rigid body motion leading to a solvable system. The

DOI: 10.1002/nme

proposed average boundary condition method has been shown to achieve machine accuracy for mode 1 crack propagation irrespective of element size for a cross crack problem.

ACKNOWLEDGEMENTS

This work was supported by the Engineering and Physical Sciences Research Council [grant number EP/K502832/1].

REFERENCES

1. R. Abedi, M.A. Hawker, R.B. Haber, and K. Matou. An adaptive spacetime discontinuous Galerkin method for cohesive models of elastodynamic fracture. International Journal for Numerical Methods in Engineering, 81(10):1207–1241, 2010.
2. W. Ai and C.E. Augarde. An adaptive cracking particle method for 2d crack propagation. International Journal for Numerical Methods in Engineering, 108(13):1626–1648, 2016. nme.5269.
3. D. Arnold. An interior penalty finite element method with discontinuous elements. SIAM Journal on Numerical Analysis, 19(4):742–760, 1982.
4. D. Arnold, F. Brezzi, B. Cockburn, and D. Marini. Unified analysis of discontinuous Galerkin methods for elliptic problems. SIAM Journal on Numerical Analysis, 39(5):1749–1779, 2002.
5. A Arranz, N Petrinic, and E Süli. Discontinuous element approximation for dynamic fracture. In Computational Plasticity: Fundamentals and Applications-Proceedings of the 8th International Conference on Computational Plasticity, COMPLAS VIII, number PART 1, pages 545–548, 2005.
6. R.S. Barsoum. Triangular quarter-point elements as elastic and perfectly-plastic crack tip elements. International Journal for numerical Methods in engineering, 11(1):85–98, 1977.
7. F. Bassi and S. Rebay. A high-order accurate discontinuous finite element method for the numerical solution of the compressible Navier–Stokes equations. Journal of Computational Physics, 131(2):267–279, 1997.
8. T. Belytschko and T. Black. Elastic crack growth in finite elements with minimal remeshing. International journal for numerical methods in engineering, 45(5):601–620, 1999.
9. P-O. Bouchard, F. Bay, and Y. Chastel. Numerical modelling of crack propagation: automatic remeshing and comparison of different criteria. Computer Methods in Applied Mechanics and Engineering, 192(35):3887–3908, 2003.
10. H.G. deLorenzi. On the energy release rate and the J-integral for 3-D crack configurations. International Journal of Fracture, 19:183–193, 1982.
11. R. Denzer, F. J. Barth, and P. Steinmann. Studies in elastic fracture mechanics based on the material force method. International Journal for Numerical Methods in Engineering, 58:1817–1835, 2003.
12. R. Denzer and A. Menzel. Configurational forces for quasi-incompressible large strain electro-viscoelasticity application to fracture mechanics. European Journal of Mechanics - A/Solids, 48:3 – 15, 2014. Frontiers in Finite-Deformation Electromechanics.
13. Ph. Destuynder, M. Djaoua, and S. Lescure. Quelques remarques sur la mécanique de la rupture élastique. Journal de Mécanique Théorique et Appliquée, 2(1):113–135, 1983.
14. F. Erdogan and G.C. Sih. On the crack extension in plates under plane loading and transverse shear. Journal of Basic Engineering, 85(4):519–525, 1963.
15. J. D. Eshelby. The force on an elastic singularity. Philosophical Transactions of the Royal Society A, 224:87–112, 1951.
16. J.D. Eshelby. Energy relations and the energy-momentum tensor in continuum mechanics. In Fundamental Contributions to the Continuum Theory of Evolving Phase Interfaces in Solids: A Collection of Reprints of 14 Seminal Papers, pages 82–119. Springer Berlin Heidelberg, Berlin, Heidelberg, 1999.
17. M. Fagerström and R. Larsson. Theory and numerics for finite deformation fracture modelling using strong discontinuities. International Journal for Numerical Methods in Engineering, 66(6):911–948, 2006.
18. E. Gürses and C. Miehe. A computational framework of three-dimensional configurational-force-driven brittle crack propagation. Computer Methods in Applied Mechanics and Engineering, 198(15):1413–1428, 2009.
19. M.E. Gurtin. Configurational forces as basic concepts of continuum physiscs. Springer-Verlag, New York, 2000.
20. M.E. Gurtin and P. Podio-Guidugli. Configurational forces and the basic laws for crack propagation. Journal of the Mechanics and Physics of Solids, 44:905–927, 1996.
21. A. Hansbo and P. Hansbo. An unfitted finite element method, based on Nitsche's method, for elliptic interface problems. Computer Methods in Applied Mechanics and Engineering, 191(47):5537–5552, 2002.
22. A. Hansbo and P. Hansbo. A finite element method for the simulation of strong and weak discontinuities in solid mechanics. Computer Methods in Applied Mechanics and Engineering, 193(33):3523–3540, 2004.
23. P. Hansbo and M. G. Larson. Energy norm a posteriori error estimates for discontinuous Galerkin approximations of the linear elasticity problem. Computer Methods in Applied Mechanics and Engineering, 200(45):3026–3030, 2011.
24. P. Heintz. On the numerical modelling of quasi-static crack growth in linear elastic fracture mechanics. International Journal for Numerical Methods in Engineering, 65(2):174–189, 2006.
25. P. Heintz, F. Larsson, P. Hansbo, and K. Runesson. Adaptive strategies and error control for computing material forces in fracture mechanics. International Journal for Numerical Methods in Engineering, 60(7):1287–1299, 2004.

26. T.K. Hellen. On the method of virtual crack extensions. International Journal for Numerical Methods in Engineering, 9(1):187–207, 1975.
27. T.K. Hellen and W.S. Blackburn. The calculation of stress intensity factors for combined tensile and shear loading. International Journal of Fracture, 11(4):605–617, 1975.
28. H. Huang and F. Costanzo. On the use of space-time finite elements in the solution of elasto-dynamic fracture problems. International Journal of Fracture, 127(2):119–146, 2004.
29. G.R. Irwin. Analysis of stresses and strains near the end of a crack traversing a plate. SPIE Milestone Series MS, 137:167–170, 1957.
30. G.R. Irwin. Linear fracture mechanics, fracture transition, and fracture control. Engineering Fracture Mechanics, 1(2):241–257, 1968.
31. H. Ishikawa, H. Kitagawa, and H. Okamura. J-integral of a mixed mode crack and its application. Mechanical Behaviour of Materials, pages 447–455, 1980.
32. R.S. Jonathan. Adaptive precision floating-point arithmetic and fast robust geometric predicates. Discrete & Computational Geometry, 18(3):305–363, October 1997.
33. Ł. Kaczmarczyk, M.M. Nezhad, and C. Pearce. Three-dimensional brittle fracture: configurational-force-driven crack propagation. International Journal for Numerical Methods in Engineering, 97(7):531–550, 2014.
34. R. Kienzler and G. Herrmann. Mechanics in material space with applications to defect and fracture mechanics. Springer-Verlag, New York, 2000.
35. E. Kuhl, H. Askes, and P. Steinmann. An ALE formulation based on spatial and material settings of continuum mechanics. Part 1: Generic hyperelastic formulation. Computer Methods in Applied Mechanics and Engineering, 193(39):4207–4222, 2004.
36. E. Kuhl, R. Denzer, F.J. Barth, and P.R. Denzer. Application of the material force method to thermo-hyperelasticity. Computer Methods in Applied Mechanics and Engineering, 193(3032):3303 – 3325, 2004. Computational Failure Mechanics.
37. R. Larsson and M. Fagerström. A framework for fracture modelling based on the material forces concept with XFEM kinematics. International Journal for Numerical Methods in Engineering, 62(13):1763–1788, 2005.
38. G.A. Maugin. Material force: concepts and applications. Applied Mechanics Reviews, 23:213–245, 1995.
39. G.A. Maugin and C. Trimarco. Pseudomomentum and material forces in nonlinear elaelastic: Variational formulations and applications to brittle fracture. Acta Mechanica, 94:1–28, 1992.
40. Gérard A Maugin. Configurational forces: thermomechanics, physics, mathematics, and numerics. CRC Press, 2016.
41. A. Menzel, R. Denzer, and P. Steinmann. Material forces in computational single-slip crystal-plasticity. Computational Materials Science, 32(34):446 – 454, 2005. {IWCMMIWCMM}.
42. J. Mergheim, E. Kuhl, and P. Steinmann. A hybrid discontinuous Galerkin/interface method for the computational modelling of failure. Communications in numerical methods in engineering, 20(7):511–519, 2004.
43. C. Miehe and E. Gürses. A robust algorithm for configurational-force-driven brittle crack propagation with R-adaptive mesh alignment. International Journal for Numerical Methods in Engineering, 72(2):127–155, 2007.
44. C. Miehe, E. Gürses, and M. Birkle. A computational framework of configurational-force-driven brittle fracture based on incremental energy minimization. International Journal of Fracture, 145(4):245–259, 2007.
45. R. Mueller, S. Kolling, and D. Gross. On configurational forces in the context of the finite element method. International Journal for Numerical Methods in Engineering, 53(7):1557–1574, 2002.
46. R. Mueller and G.A. Maugin. On material forces and finite element discretizations. Computational Mechanics, 29(1):52–60, 2002.
47. B. Näser, M. Kaliske, H. Dal, and Ch. Netzker. Fracture mechanical behaviour of visco-elastic materials: application to the so-called dwell-effect. ZAMM-Journal of Applied Mathematics and Mechanics/Zeitschrift für Angewandte Mathematik und Mechanik, 89(8):677–686, 2009.
48. B. Näser, M. Kaliske, and R. Müller. Material forces for inelastic models at large strains: application to fracture mechanics. Computational Mechanics, 40(6):1005–1013, 2007.
49. V. P. Nguyen. Discontinuous Galerkin/extrinsic cohesive zone modeling: Implementation caveats and applications in computational fracture mechanics. Engineering Fracture Mechanics, 128:37–68, 2014.
50. W. Ochensberger and O. Kolednik. A new basis for the application of the $$j$$ j -integral for cyclically loaded cracks in elastic–plastic materials. International Journal of Fracture, 189(1):77–101, 2014.
51. K. Özenç, M. Kaliske, G. Lin, and G. Bhashyam. Evaluation of energy contributions in elasto-plastic fracture: a review of the configurational force approach. Engineering Fracture Mechanics, 115:137–153, 2014.
52. K. Park and G.H. Paulino. Cohesive zone models: a critical review of traction-separation relationships across fracture surfaces. Applied Mechanics Reviews, 64(6):060802–060802–20, 2011.
53. D.M. Parks. A stiffness derivative finite element technique for determination of crack tip stress intensity factors. International Journal of Fracture, 10(4):487–502, 1974.
54. D.M. Parks. The virtual crack extension method for nonlinear material behavior. Computer Methods in Applied Mechanics and Engineering, 12(3):353–364, 1977.
55. D.M. Parks. Virtual crack extension-A general finite element technique for J-integral evaluation. Numerical Methods in Fracture Mechanics, pages 464–478, 1978.
56. T. Pin and T.H.H. Pian. On the convergence of the finite element method for problems with singularity. International Journal of solids and Structures, 9(3):313–321, 1973.
57. M. Prechtel, P.L. Ronda, R. Janisch, A. Hartmaier, G. Leugering, P. Steinmann, and M. Stingl. Simulation of fracture in heterogeneous elastic materials with cohesive zone models. International Journal of Fracture, 168(1):15–29, 2011.
58. R. Radovitzky, A. Seagraves, M. Tupek, and L. Noels. A scalable 3D fracture and fragmentation algorithm based on a hybrid, discontinuous Galerkin, cohesive element method. Computer Methods in Applied Mechanics and Engineering, 200(1):326–344, 2011.

DOI: 10.1002/nme

59. W.H. Reed and T.R. Hill. Triangular mesh methods for the neutron transport equation. Los Alamos Report LA-UR-73-479, 1973.
60. J.R. Rice. A path independent integral and the approximate analysis of strain concentration by notches and cracks. Journal of Applied Mechanics, 35:379–386, 1968.
61. G.R. Richter. The discontinuous Galerkin method with diffusion. Mathematics of Computation, 58(198):631–643, 1992.
62. A.L. RicMenzel, J. Hegemann, E. Sifakis, J. Hellrung, and J.M. Teran. An xfem method for modeling geometrically elaborate crack propagation in brittle materials. International Journal for Numerical Methods in Engineering, 88(10):1042–1065, 2011.
63. K. Runesson, F. Larsson, and P. Steinmann. On energetic changes due to configurational motion of standard continua. International Journal of Solids and Structures, 46(6):1464–1475, 2009.
64. M. Scherer, R. Denzer, and P. Steinmann. On a solution strategy for energy-based mesh optimization in finite hyperelastostatics. Computer Methods in Applied Mechanics and Engineering, 197(6):609–622, 2008.
65. C. Schwab. p-and hp-finite element methods: Theory and applications in solid and fluid mechanics. Oxford University Press, 1998.
66. Yongxing Shen and Adrian Lew. An optimally convergent discontinuous galerkin-based extended finite element method for fracture mechanics. International Journal for Numerical Methods in Engineering, 82(6):716–755, 2010.
67. G.C. Sih and B. Macdonald. Fracture mechanics applied to engineering problems-strain energy density fracture criterion. Engineering Fracture Mechanics, 6(2):361–386, 1974.
68. P. Solin, K. Segeth, and I. Dolezel. Higher-order finite element methods. CRC Press, 2003.
69. P. Steinmann, D. Ackermann, and F. J. Barth. Application of material forces to hyperelastostatic fracture mechanics. ii. Computational setting. International Journal of Solids and Structures, 38:5509–5526, 2001.
70. P. Steinmann and G.A. Maugin, editors. Mechanics of material forces. Springer-Verlag, 2005.
71. H. Stumpf and K. C. Le. Variational principles of nonlinear fracture mechanics. Acta Mechanica, 83:25–37, 1990.
72. N. Sukumar and T. Belytschko. Arbitrary branched and intersecting cracks with the extended finite element method. International Journal for Numerical Methods in Engineering, 48:1741–1760, 2000.
73. H. Tada, P.C. Paris, and G.R. Irwin. The stress analysis of cracks. Del Research Corp, Hellertown PA, 1973.
74. J. Tago, V. M. Cruz-Atienza, J. Virieux, V. Etienne, and F. J. Snchez-Sesma. A 3D hp-adaptive discontinuous Galerkin method for modeling earthquake dynamics. Journal of Geophysical Research: Solid Earth, 117(B9), 2012.
75. P. Thoutireddy and M. Ortiz. A variational r-adaption and shape-optimization method for finite-deformation elasticity. International Journal for Numerical Methods in Engineering, 61(1):1–21, 2004.
76. J. Tillberg, F. Larsson, and K. Runesson. On the role of material dissipation for the crack-driving force. International Journal of Plasticity, 26(7):992–1012, 2010.
77. L. Wu, G. Becker, and L. Noels. Elastic damage to crack transition in a coupled non-local implicit discontinuous Galerkin/extrinsic cohesive law framework. Computer Methods in Applied Mechanics and Engineering, 279:379–409, 2014.
78. A.M. Yan and H. Nguyen-Dang. Multiple-cracked fatigue crack growth by BEM. Computational Mechanics, 16(5):273–280, 1995.